JOURNAL OF GEOPHYSICAL RESEARCH: SPACE PHYSICS, VOL. 118, 3866–3876, doi:10.1002/jgra.50212, 2013

Low latitude thermospheric responses to magnetic storms

G. D. Earle,[1] R. L. Davidson,[1] R. A. Heelis,[2] W. R. Coley,[2] D. R. Weimer,[1] J. J. Makela,[3] D. J. Fisher,[3] A. J. Gerrard,[4] and J. Meriwether[5]

Received 21 November 2012; revised 10 February 2013; accepted 4 March 2013; published 24 June 2013.

[1] Thermospheric density and neutral velocity perturbations associated with three magnetic storms in the autumn season of 2011 are examined using data from the neutral wind meter (NWM) on the Communication/Navigation Outage Forecast System (C/NOFS) satellite. The data from perigee passes near 400 km altitude show marked increases in neutral density during the storms and associated increases in horizontal neutral flow speeds. These thermospheric responses are characterized by enhanced meridional neutral flows with peak perturbation amplitudes near 100 m/s and relative neutral density enhancements ranging from 50–100%. The increases in the neutral density and meridional flow velocity at equatorial latitudes occur about 5–7 h after the initial perturbations are observed in the *z* component of the interplanetary magnetic field (IMF), and they persist for 20–30 h. The perturbations in the neutral density are in good agreement with temperature increases predicted by an empirical model that has been validated using data from the CHAMP and Gravity Recovery and Climate Experiment missions, with a maximum lag time of ~1–1.5 h between the model temperature increases and the observed density perturbations. The model temperatures are in excellent agreement with ground-based low-latitude temperature measurements during the storms. Ground-based wind measurements during one of the storms provide additional data for comparison with the perturbation wind amplitudes measured aboard the satellite.

Citation: Earle, G. D., R. L. Davidson, R. A. Heelis, W. R. Coley, D. R. Weimer, J. J. Makela, D. J. Fisher, A. J. Gerrard, and J. Meriwether (2013), Low latitude thermospheric responses to magnetic storms, *J. Geophys. Res. Space Physics*, *118*, 3866–3876, doi:10.1002/jgra.50212.

1. Introduction

[2] Energy carried by enhanced particle precipitation and electromagnetic fields is injected into the high-latitude regions of the Earth's ionosphere during magnetic storms. The subsequent enhancements in the auroral current systems heat both the charged particles in the ionosphere and the neutral thermospheric particles, and the resulting expansion of both the thermosphere and ionosphere changes the distribution of their particle densities with respect to both latitude and altitude. *Balan et al*. [2011] provide examples of latitudinal changes in the ion and neutral densities during storms. Their data are from altitudes near 400 km on the high-inclination CHAMP satellite during 2000–2003. They argue that their observations are consistent with mechanical effects created by enhanced equatorward neutral flows occurring simultaneously in both hemispheres during the storms. *Deng et al*. [2011] use a general circulation model to study the altitude dependence of Joule heating effects during storms. They find that the Joule heating per unit mass maximizes in the F region of the ionosphere, and that heating at altitudes above ~150 km is the dominant source of thermospheric density increases at altitudes greater than 300 km. In addition to purely mechanical effects, chemical changes that modify the composition and the O/N_2 ratio also result from storms; these changes begin at high latitudes and propagate to the equatorial regions in periods as short as 1.5–2.5 h [*Liu and Luhr*, 2005].

[3] Abrupt variations in the interplanetary electric field (IEF) during magnetic storms also penetrate directly to low latitudes, where they modify the equatorial electric field and the associated current systems [*Rastogi*, 1977]. *Gonzales et al*. [1979] show that the structured zonal electric field at auroral latitudes has features identical to those seen in the equatorial vertical drifts measured at the Jicamarca observatory. A subsequent extension of this study by *Earle and Kelley* [1987] shows that changes in the solar wind on time scales less than ~1 h are not effectively shielded by the ring current, so they appear as strong noise sources in the equatorial electric field for $K_p > 3^+$. Currents associated with these enhanced electric fields may also contribute to storm-induced heating at low latitudes.

[4] The focus of this paper is to present *in situ* data that characterize the temporal response of the low latitude thermospheric neutral density and drift during three moderate

[1]Virginia Tech, Blacksburg, Virginia, USA.
[2]The University of Texas at Dallas, Richardson, Texas, USA.
[3]The University of Illinois, Champaign, Illinois, USA.
[4]New Jersey Institute of Technology, Newark, New Jersey, USA.
[5]Clemson University, Clemson, South Carolina, USA.

Corresponding author: G. D. Earle, Virginia Tech, 1901 Innovation Drive, Suite 1000, Space@VT, Virginia Tech, Blacksburg, VA 24060, USA (earle@vt.edu)

2169-9380/13/10.1002/jgra.50212

storms in late 2011. We show that the density perturbations observed by the satellite instrumentation are consistent with both the temperature fluctuations observed in the lower thermosphere by ground-based systems, and with modeled storm-time temperature increases at equatorial latitudes. The local times of perigee for the satellite are quite different at the onset of each storm studied here, so the local time period sampled throughout the onset and recovery phase of the storms is unique in each case. All three storms have similar Dst features, but the neutral density and velocity measurements made by the satellite near 400 km altitude show distinct and significant differences in their relative magnitudes and their temporal responses. Ground-based data from lower altitudes are available for comparison with the measured storm responses. Modeled thermospheric temperature and density changes are presented for comparison in all three cases.

2. In Situ Instrument System

[5] The Coupled Ion-Neutral Dynamics Investigation (CINDI) is a NASA mission of opportunity comprising four separate sensors aboard the C/NOFS satellite. The mission was launched on 16 April 2008 into an elliptical orbit with a 13° inclination, 850 km apogee, and perigee near 400 km. It completes ~15 orbits per day, and samples all local times at perigee over a period of approximately 2 months. During the early phases of the CINDI mission, the neutral atmospheric density at perigee altitudes was very low, and the composition was dominated by neutral helium [*Haaser et al*., 2010]. These conditions are detrimental to the signal-to-noise ratios in the CINDI wind instruments, effectively preventing the neutral wind instrumentation from making high-resolution measurements. Increasing solar irradiance throughout 2011 produced larger neutral temperatures and densities at C/NOFS perigee altitudes, so by the end of 2011 the signal-to-noise ratios of the neutral instrumentation were sufficient to allow more reliable measurements, particularly during storm periods.

[6] The satellite data shown in this paper are from the cross-track sensor (CTS) of the neutral wind meter (NWM), which is based on a concept proposed by *Hanson et al*. [1992] and validated on several sounding rocket flights [*Earle et al*., 2010]. The instrument is designed to measure pressure differences created by winds in the two directions perpendicular to the motion of the satellite; for C/NOFS, one of these directions is vertical and the other is predominantly in the north-south direction. Due to power limitations and other operational issues on the C/NOFS satellite, only the north-south channel was powered and operational during the storm events presented here. This precludes the possibility of vector measurements of neutral drifts during the storms, so all of the velocity enhancements shown here are presented in the spacecraft coordinate system.

[7] The basic operating principle for the CTS is to measure small pressure differentials created within the instrument by the bulk motions of the thermal neutral gas [*Hanson et al*., 1992]. The instrument faces in the ram direction and the four apertures on its hemispherical cover are situated 22.5° from the ram-pointing axis. The pressure measured in four cavities behind these apertures is related to the arrival angle of the neutral gas relative to each aperture normal. When combined with detailed knowledge of the vehicle velocity vector, the pressure differentials between diametrically opposed cavities allow the cross-track wind speed to be determined in the satellite frame of reference.

Table 1. Locations of the Ground-Based Observatories in Peru and Brazil From Which Storm-Time Data Are Available for Comparison With the Satellite Observations

Ground-Based Site Identifier	Geographic Latitude	Geographic Longitude
RENOIR-Merihill	−11.96°	−76.86°
RENOIR-Nazca	−14.97°	−74.89°
RENOIR-Cajazeiras	−6.87°	−38.56°
RENOIR-Cariri	−7.38°	−36.53°
SOFDI	−12.0°	−75.2°

[8] Ion gages within the CTS are used to measure the pressure in flight, and changes in these neutral pressures along the orbit track near perigee are proxies for spatial and/or temporal fluctuations in the neutral density because the relative pressure ratios are not sensitive to the ambient neutral temperature. Thus, the CTS pressure measurements are the basis for both the wind speed and neutral density fluctuations presented here.

[9] Uncertainties in the CTS measurements stem from several different sources. First, small alignment errors during instrument installation on the satellite coupled with pointing errors in satellite attitude control yield uncertainties in the velocity measurements of approximately 10 m/s. This situation is largely mitigated in the present study, since we limit our attention to perturbation quantities rather than absolutes. The second source of error is due to noise in the instrument electronics; in some cases, these errors cannot be distinguished from small geophysical variations, and these uncertainties influence both absolute and relative measurements of densities and velocities in the medium. Error bars on the graphs shown in this paper are representative of the magnitude of these uncertainties.

3. Ground-Based Systems

[10] Table 1 shows the geographical locations of the ground-based observatories used for comparison with the satellite data. These observatories include elements of systems known collectively as RENOIR and SOFDI.

3.1. RENOIR

[11] For comparison with the storm-time satellite observations and models, temperature measurements from ground sites in the South American sector are available from Fabry-Perot interferometers (FPIs) that comprise the Remote Equatorial Nighttime Observatory of Ionospheric Regions (RENOIR) experiments. Five Fabry-Perot interferometer (FPI) observatories operated during the August storm in both Peru and northeastern Brazil. One of these, located at Huancayo, Peru, made daytime and nighttime measurements of thermospheric winds. The other four, located at Jicamarca and Nazca in Peru and Cajazeiras and Cariri in Brazil, observe thermospheric winds and temperatures only at night. All of these instruments are imaging FPIs that use a charge-coupled device camera as the detector. The details of the instrumentation and data analysis methods are provided by *Gerrard and Meriwether* [2011], *Meriwether et al*. [2011],

and *Makela et al*. [2011]. The two FPI observatories in northeastern Brazil are part of the RENOIR system [*Makela et al*., 2009].

[12] The FPIs comprising the RENOIR system measure thermospheric neutral temperatures and winds by observing broadening and Doppler shifts from the 630.0-nm redline emission. The peak brightness of this emission occurs near 230 km and is caused by dissociative recombination of O_2^+ in the broad oxygen layer in the thermosphere between ~200 km and ~300 km [*Solomon and Abreu*, 1989; *Zhang and Shepherd*, 2004]. The intensity of this signal can be affected by changes in both the plasma and neutral conditions. For example, if the plasma concentration decreases the reduced number of O_2^+ ions will cause the intensity of the signal to decrease. However, the signal can also decrease due to changes in the neutral gas background relative to the plasma. For instance, if the F-region plasma is lifted to higher altitudes relative to the neutral background (e.g., by electric fields), then the number of neutral particles will decrease relative to the plasma density due to the exponential decay of the thermospheric density with altitude. This lowers the dissociative recombination rate of O_2^+, which in turn decreases the signal intensity [*Makela et al*., 2001].

[13] The FPI collects line of sight emission data from any point in the sky by using a dual-mirror pointing system with two computer-controlled motors; one mirror is used for azimuthal rotation and the other for elevation. It has a pointing accuracy within ~0.2° and a field-of-view of 1.8°, which provides an image area approximately 8 km wide at the emission height. Four to five-minute integrations are used to collect data from each desired direction, and a 30 s laser exposure is taken every cycle. One of the more common modes of observation utilizes 45° elevation-angle observations to the north, east, south, and west, coupled with a zenith measurement. The system and its operating modes are described in more detail in *Makela et al*. [2009] and *Meriwether et al*. [2011].

[14] The FPI imager collects the emission in the form of an Airy interference pattern created by the etalon. This two-dimensional pattern is condensed by radial summation to form a one-dimensional fringe pattern. Each fringe is then analyzed individually as the convolution of the instrument function (deduced from the laser image) and a modeled Gaussian source for the emission. Using a nonlinear least squares algorithm to solve for the optimal source parameters, a temperature estimate is derived from the width of the fitted Gaussian, along with an estimate of the uncertainty in that parameter [*Makela et al*., 2011]. For typical conditions, the estimated uncertainty in the calculated temperatures is approximately 25 K, but it can increase due to decreases in signal intensity. It is assumed that the temperature is uniform across the visible sky when averaging these data.

3.2. SOFDI

[15] Neutral velocity data during the August storm are available from the Second-generation, Optimized, Fabry-Perot Doppler Imager (SOFDI) system. These data are from the geomagnetic equatorial region at Huancayo, Peru. SOFDI is a triple-etalon Fabry-Perot interferometer (FPI) capable of making wind and temperature measurements over a full 24-h period from the spectra obtained for a variety of upper atmospheric emission lines. As presented herein, SOFDI uses the same emission wavelength used by the RENOIR system. The instrument makes measurements in the cardinal directions at a 60° zenith angle to infer zonal and meridional winds and temperatures. A vertical look direction is used as a Doppler reference, and a He-Ne laser is used to determine the instrument function. Nighttime measurements use a single etalon and the SOFDI instrument works like a traditional "nighttime-only" FPI system. Daytime measurements use all three etalons in conjunction and require a solar reference spectrum from which the OI dayglow is extracted. A full description of the instrument capabilities, data processing methods, and initial data, as well as a full treatment of instrument limitations, is presented in *Gerrard and Meriwether* [2011].

[16] The August 2011 SOFDI measurements reported herein were taken under extremely clear atmospheric conditions and at a high level of system performance. Data from the nominal data samples (20-min at night, 5-min during the day) were uniformly binned into 1-h values, taking into account statistical uncertainty and geophysical variability. The uncertainty bars were never allowed to go below 10 m/s due to the inherent assumptions in the FPI methodology listed above.

[17] Interpretation of FPI measurements must be looked at with care because of particulars associated with the measurement technique. For example, the wind and temperature measurements stem from a layer-integrated Gaussian-like emission profile taken at a slant profile. Thus, the values should be thought of as horizontally and vertically "smeared" values. In addition, it is often assumed that the OI emission layer is constant in height and time during the data collection. However, this is certainly not the case and can be quite dramatic during high geomagnetic activity when upward equatorial motion raises the emission layer and reduces the emission intensity; often to the point where the emission disappears. This can make the interpretation of measurements during geomagnetic storms difficult.

4. Model Temperatures

[18] Model temperature data from 400 km altitude are available for comparison with the observed density perturbations and ground-based temperature measurements during the storms. For each storm studied, an empirical model [*Weimer*, 2005b] is used to obtain the total Joule heating in both polar caps, from which temperature changes in the thermosphere are derived. This empirical model actually consists of two models in combination. The first model provides the polar cap electric potentials as a function of position in geomagnetic latitude and magnetic local time (MLT) using modified apex coordinates [*Richmond*, 1995]. The input values required by the model are the IMF magnitude and angle in the *Y-Z* plane in geocentric solar magnetic (GSM) coordinates [*Hapgood*, 1992], the solar wind velocity and density, and the dipole tilt angle. This angle is the rotation between the GSM and solar magnetic (SM) coordinate systems. The model is based on electric field measurements from the polar-orbiting DE-2 satellite, with solar wind/IMF measurements from IMP-8 and ISEE-3. The other, twin model is derived from magnetometer measurements on the same DE-2 satellite, originally for the purpose of mapping field-aligned currents through the use of magnetic Euler potentials [*Weimer*, 2001]. It was later

Table 2. Wind Data From the HWM-07 Model [*Drob et al.*, 2008] and Neutral Density Data From the MSIS-E90 Model [*Hedin*, 1991] Averaged Over the Local Time Intervals Corresponding to Each Storm Event

Storm Period	Average Meridional Model Wind	Average Model Density
August	−42.26 m/s	6.25×10^7 cm^{-3}
September	−21.5 m/s	1.63×10^8 cm^{-3}
October	62.01 m/s	8.94×10^7 cm^{-3}

determined that the gradients of the magnetic Euler potentials could be combined with the electric fields in order to derive the Poynting flux and Joule heating [*Weimer*, 2005a]. The most recent version of the combined model [*Weimer*, 2005b], hereafter referred to as W05, uses Spherical Cap Harmonic Analysis [*Haines*, 1985] and has a spherical cap boundary that expands and contracts as the IMF changes.

[19] It has been found that the total heating calculated with this model has a high correlation with changes in the temperature of the thermosphere, as derived from neutral density measurements on both the CHAMP and GRACE satellites [*Weimer et al*., 2011]. The Jacchia-Bowman 2008 model [*Bowman et al*., 2008] is used to derive changes in the global average thermospheric temperature from these density measurements; these temperature changes due to auroral heating are perturbations to the more slowly varying background level that results from absorption of solar radiation, in equilibrium with heat losses. The effects of both precipitation-induced heating and solar flares are included in this model, through inclusion of a parameter called Y10 [*Bowman et al*., 2008]. When the level of auroral heating is reduced, the temperature perturbations decline at an exponential rate. Through a comparison of the total auroral heating power from the W05 model with the temperature perturbations that were obtained from the CHAMP and GRACE measurements, *Weimer et al*. [2011] derive a differential equation that models the temperature values. These results are used to obtain, from IMF measurements, temperature corrections that can be used in the Jacchia-Bowman 2008 model to calculate neutral densities in the global thermosphere.

5. Data Presentation

[20] The three storms of interest in this study began on days 217 (August), 269 (September), and 297 (October) of 2011. The onset times for these three storms are approximately 2000, 1500, and 2100 UT, respectively, so the orientation of the Earth's geomagnetic pole during onset is similar for the storms in August and October, but quite different for the September storm. Each storm persists for many hours, during which the satellite perigees cover all longitudes over a limited range of local times. The perigee observations sample local time periods centered near 1800, 1330, and 0000 solar local times (SLT) for the August, September, and October storms, respectively. For reference with the storm-time observations of density and velocity perturbations shown here, Table 2 provides average background

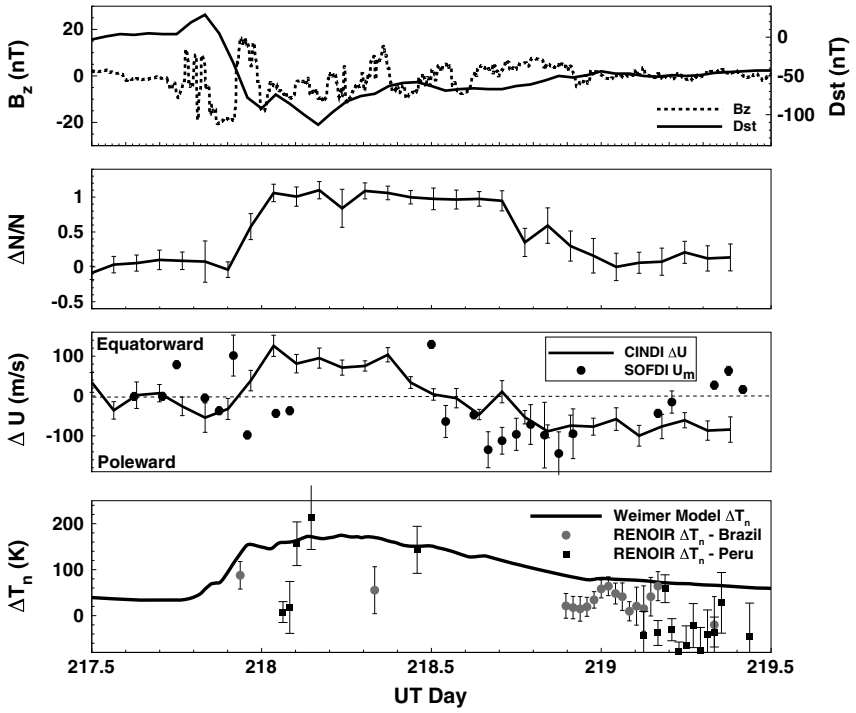

Figure 1. (top) August storm data showing the ring current Dst and IMF Bz signatures, (second panel) in situ neutral density fluctuation, (third panel) spacecraft-frame horizontal neutral velocity fluctuations superimposed with meridional thermospheric winds from SOFDI, and (bottom panel) modeled and measured temperature fluctuations. Each measured data point from the in situ observations represents a median-filtered value from a sequence of samples near perigee (400 km) for a single orbit. The solar local times sampled by the satellite for this storm covered ~1645–1900 h. The model temperature data are derived from a two-stage model seeded by the IMF values (see text).

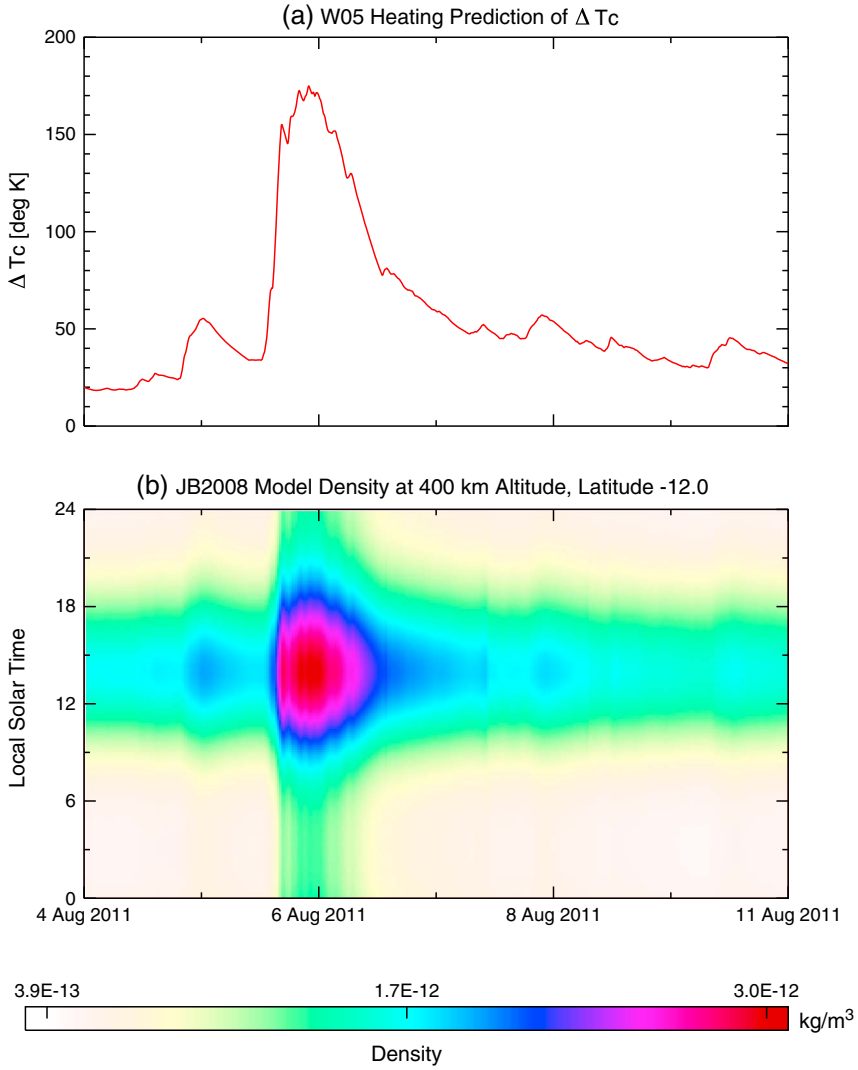

Figure 2. Results from the two-step model calculations for the August storm. Figure 2a shows the temperature change in the global average exospheric temperature, and Figure 2b shows the neutral mass density increase from this model that accompanies this change in temperature. This density is shown for all local times at -12° latitude and 400 km altitude.

conditions obtained from the MSISE-90 [*Drob et al.*, 2008] and HWM-07 [*Hedin*, 1991] models of thermospheric densities and winds, respectively. While none of the satellite observations show absolute measurements of these parameters, it is useful to know the model values of these parameters as a reference against which to interpret the magnitude of the observed perturbations.

[21] A model study by *Fuller-Rowell et al.* [1994] shows that the global distribution and evolution of storm related features varies significantly relative to the UT time of storm onset. Haaser et al. [Storm time meridional wind perturbations in the equatorial upper thermosphere, submitted to *Journal of Geophysical Research*, 2012] use thermal ion and neutral data from the C/NOFS satellite and complementary information from the ACE and WIND satellites to examine a set of storms (including the three studied here) from late 2011 and early 2012 in relation to these model predictions. The focus of the data presented here is different; our goal is to validate the thermospheric storm observations by comparing the *in situ* storm data to known physical phenomenology, empirical model temperatures, and ground-based data sets.

[22] Figure 1 shows the data from the August storm over a 48-h period that encompasses the storm onset, main phase, and recovery. The top panel shows the Dst index and IMF B_Z signature. The second and third panels show the *in situ* satellite data from the neutral wind instrument, and the bottom panel shows the model temperature perturbation near 400 km superimposed with the measured temperatures from the RENOIR systems in Brazil and Peru. SOFDI measurements of meridional neutral winds are also shown in the third panel for comparison with the in situ horizontal wind perturbations. For convenience, the velocity plot is labeled to show equatorward and poleward directions, but it is important to recognize that the true wind direction to which the satellite is sensitive depends on its direction of travel

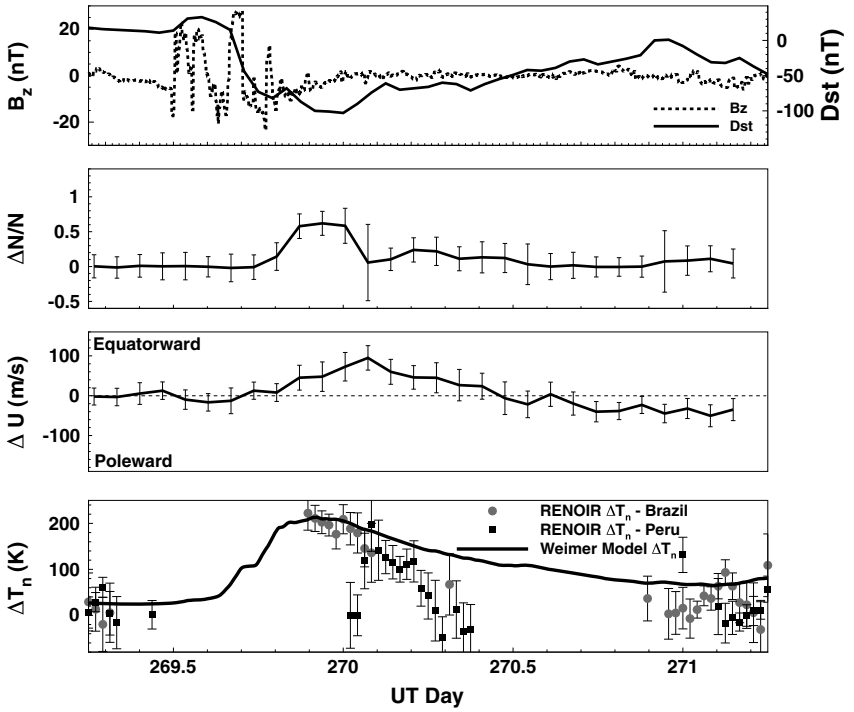

Figure 3. Data from the September storm in the same basic format as Figure 1, but without the SOFDI winds. The solar local times sampled by the satellite at perigee during this storm cover ~1215–1430 h.

along the orbit track. Since the satellite is in a low inclination orbit, the angle between the spacecraft coordinate system and the geographic system is never greater than 13°, so the axis along which the wind is measured is predominantly in the north-south direction. By coincidence, the satellite measurements during all three storm periods are from the southern hemisphere.

[23] There are several aspects of the August storm observations that are worth noting. First, the local times of satellite perigee passes occur near the sunset terminator during

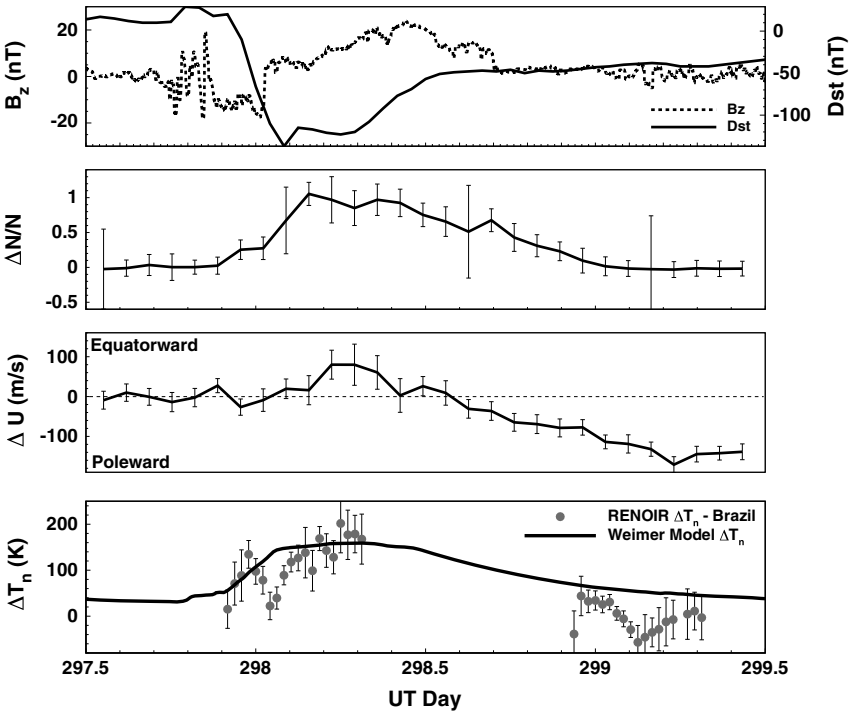

Figure 4. Data from the October storm, in the same format as Figure 3. The solar local times sampled by the satellite at perigee during this storm cover ~2250–0030 h.

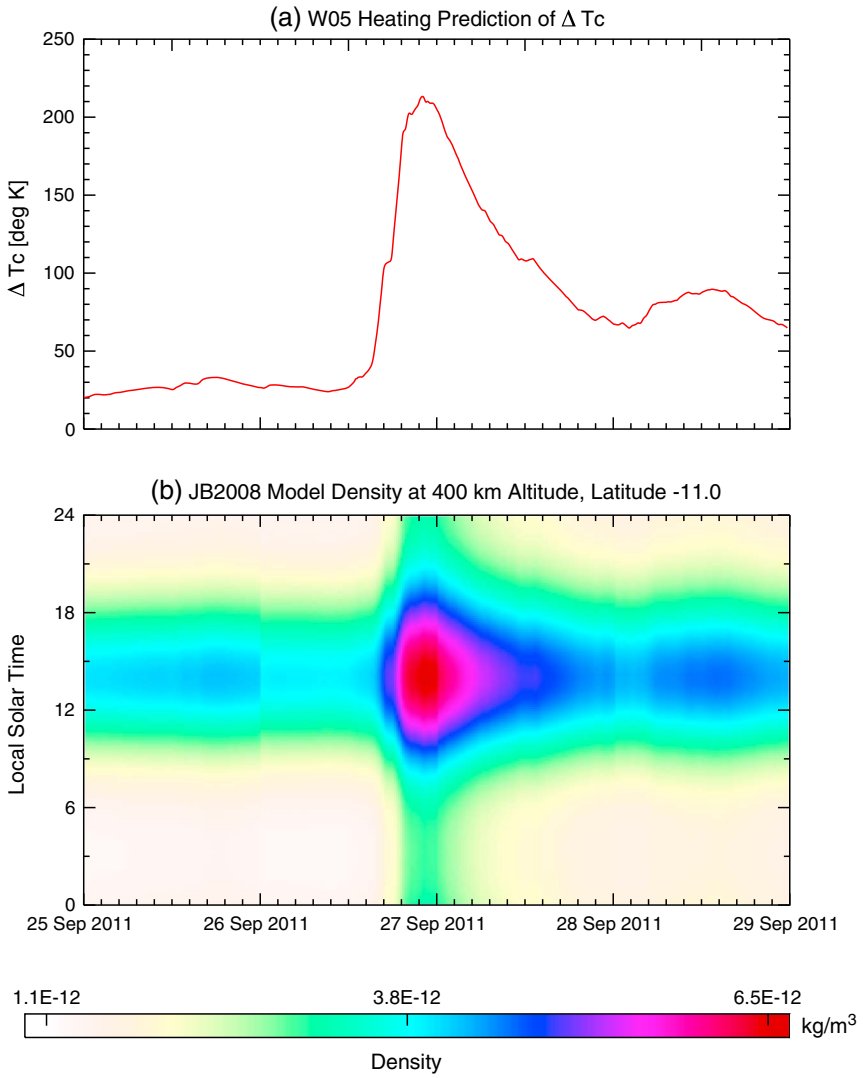

Figure 5. (a and b) Model thermospheric temperature and density data for the September storm, in the same format as Figure 2.

the storm, so conditions in the thermosphere may be undergoing diurnal variations that are independent of the storm forcing. Furthermore, the ground-based data are missing during much of the main phase of the storm, because the signals disappear shortly after storm commencement. Nevertheless, it is worthwhile to include the ground-based data for comparison with the *in situ* velocity observations and modeled thermospheric storm-induced temperature changes. Finally, the background currents measured by the CTS instrument prior to the August storm are very near the lower limit of the instrument's sensitivity, which indicates very low neutral density levels in the thermosphere at perigee altitudes. The data from the other two storms do not suffer from these shortcomings, so may be considered more reliable.

[24] Each point on the density and velocity curves in the figure corresponds to median values of the satellite measurements near perigee, so neighboring points in time correspond to perigee passes on sequential orbits. Perigee is very near 400 km for all of the data shown, but since the orbit plane is not stationary in the Earth-fixed frame, each point plotted represents observations from different latitudes, longitudes, and local times, as discussed above. In particular, we note that only a few of the perigee passes during the storm provide data taken in close spatial proximity to the ground-based observations, because over the 48-h period encompassing the storm the satellite covers all longitudes but only a few hours of local time. Each time the satellite approaches perigee it is over a position on the globe where the local time is roughly the same, but the longitude is very different. By coincidence, the first few perigee passes after the onset of the storm shown in Figure 1 were closest to the locations of the ground stations.

[25] Both the velocity and density data shown are fluctuation amplitudes, which are normalized to zero for the quiet periods at the start of each storm. The error bars are calculated as median absolute deviations from the median-filtered data near perigee altitudes for each orbit. At intermittent intervals the error bars are quite large; this occurs because of a known oscillation in the telemetered electrometer samples, which is created within the instrument electronics.

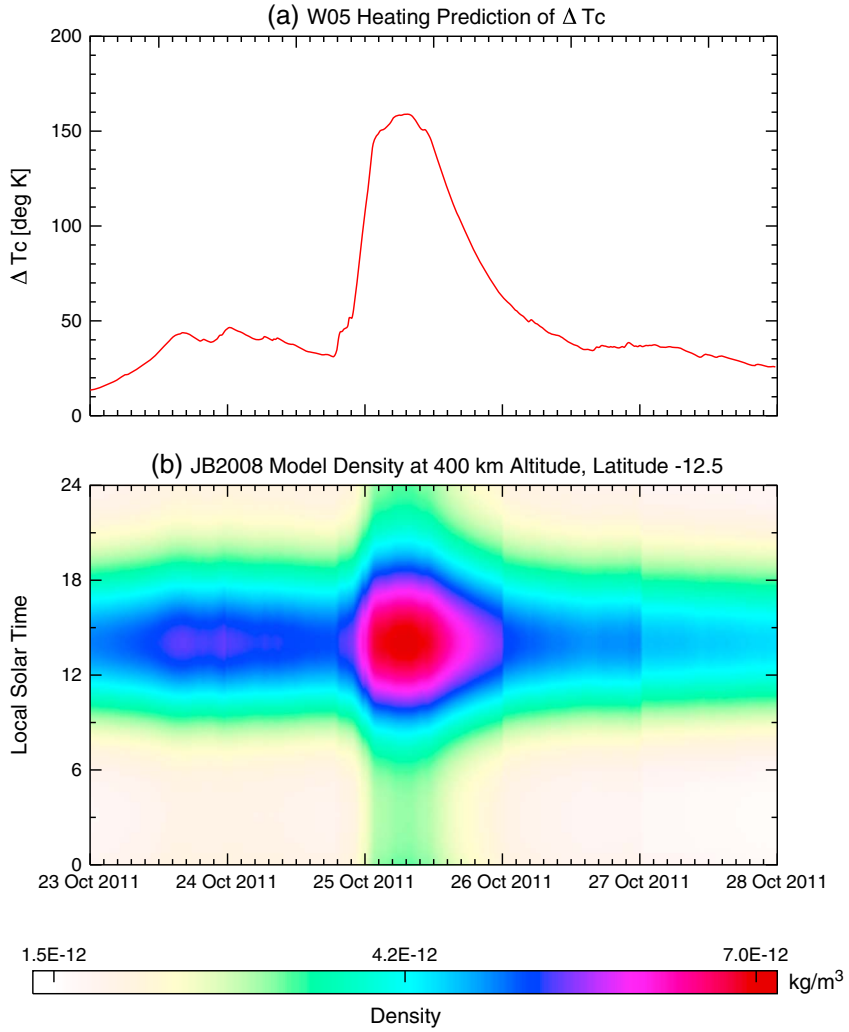

Figure 6. (a and b) Model data for the October storm in the same format as Figures 2 and 5.

[26] The model temperature data shown in the bottom panel of the figure are changes in the nighttime minimum global-average exospheric temperature. *Bowman et al.* [2008] refer to this minimum exospheric temperature as T_c. These temperature changes are derived from outputs from the W05 model using the methodology described by *Weimer et al.* [2011]. The temperature measurements at a fixed location vary with local time during the course of each day, while the ΔT_c temperatures are from modeled global averages.

[27] Figure 2 shows the results of the model calculations over a longer time scale to highlight the effects of the storm relative to the normal background variations in neutral temperature and density. The bottom panel shows the neutral mass density from the Jacchia-Bowman 2008 model at 400 km altitude (perigee) and −12° latitude (the average perigee latitude), where the model is driven by the temperature changes derived from the W05 model. These model outputs show the density at all longitudes, converted to local solar time and plotted as a function of date on the horizontal axis and local solar time on the vertical axis. The top panel in Figure 2 shows the modeled changes in the global, minimum exospheric temperature over the same range of dates. This format allows quantitative values for the modeled temperature perturbation to be more easily determined and tracked over time. These quantitative temperatures will be shown in the discussion section to be in good agreement with the density perturbations apparent in the satellite data set.

[28] Figures 3 and 4 show measured data and modeled temperatures at 400 km altitude near the equator for the September and October storms, in the same format as Figure 1. There are no SOFDI data from these storm periods, and the data from RENOIR are only from the Brazil site in Figure 4. The horizontal axes in these graphs cover 48 h, and the vertical axes in corresponding panels in Figures 1, 3, and 4 are the same in order to allow comparisons between the storm data from each period. Figures 5 and 6 show the modeled temperature and density perturbations in the same format as Figure 2. Perigees during the August storm period occur in the 1645–1900 SLT period, while for the September and October storms the SLT periods sampled are 1215–1430 and 2250–0030, respectively. Thus, the onset of the August storm occurs when the satellite perigee is near the sunset terminator, while the September and October storm onsets occur when the perigees are near local noon and midnight, respectively. These differences should

be kept in mind when comparing the plots, since the modeling study by *Fuller-Rowell et al*. [1994] indicate that the responses to storms vary as a function of longitude for storms with different UT onset times.

6. Discussion

[29] Although the three storms are different in their detailed features, their gross Dst signatures are remarkably similar. All three storms have a main phase characterized by magnetic Dst variations of at least −100 nT over periods of ~2 h. Specifically, the largest negative values of Dst attained during the August, September, and October storms are −113.3, −104.3, and −135.6 nT, respectively. The differences between the maximum and minimum Dst values are 141.7, 132.8, and 165.8 nT for the three storms, in order of occurrence. The largest gradients in Dst are also remarkably similar for all three storms. The largest rate of change occurs in September, when the Dst value has a maximum slope of −41.5 nT/h. For August, this maximum rate of change of Dst is −38.4 nT/h, while in October it is −39.5 nT/h. The elapsed times for Dst to change from its maximum to its minimum value in the August, September, and October storms are 7.9, 10.1, and 6.5 h, respectively. In each storm, the onset of higher frequency oscillations in B_Z occurs about an hour prior to the compression phase that precedes the main phase of the storm.

[30] Regarding the ionospheric/thermospheric responses, in all three cases the thermospheric density near the equator increases by 50% or more within a few hours of the onset of the storm. Although the neutral flow vector cannot be unambiguously determined during the storm events for reasons described earlier, in all three cases the observations are consistent with strong increases in equatorward flows that commence during the main phases of the storms. Another very noticeable similarity is evident in the velocity perturbation measurements. In all three cases, the neutral flow velocity perturbation is initially equatorward, but changes to poleward about 20 h after the onset of the storm.

[31] Of particular interest is the August storm in which the measured meridional wind at ~400 km can be compared with ground-based SOFDI winds from ~230 km during the day and into the night of day 219. Although nighttime data from day 218 are not available due to the greatly weakened emission intensity, integration of the signal over the entire night yields an averaged nighttime meridional velocity of 70 m/s ± 20 m/s (i.e., equatorward), which is consistent with the CTS measurement. The meridional winds measured at lower altitudes with the SOFDI system are very similar in magnitude and direction, which is expected given the viscosity of the thermosphere. However, at the lower altitudes the ground-based measurements deviate from the CTS perturbation winds at ~00 UT on day 219, switching direction completely. An extended temporal view [not shown] shows a "damped oscillator" structure in the meridional wind lasting ~3 days, with a period of ~1.2 days [A. J. Gerrard, et al., Equatorial thermospheric winds Q5 measured during the August 2011 storm, submitted to *Geophysical Research Letters*, 2012]. We speculate that this motion is associated with the initial equatorward and lifting motion of the lower thermosphere associated with the storm, with subsequent rebound and overshoot as the system restabilizes. Unfortunately, no SOFDI data were available from the September or October storms to confirm this hypothesis. Modeling of the equatorial thermospheric response to such storm-time driving should be able to verify this process. Zonal wind measurements from SOFDI during and after the storm were relatively unremarkable.

[32] For the September and October storms, the thermospheric temperature perturbations measured by the RENOIR ground-based system closely match the predictions of the empirical model. Unfortunately, the data quality during the August storm was insufficient to obtain good ground-based temperature measurements during the main phase of the storm. This is not surprising since the *in situ* data revealed exceptionally low neutral densities near perigee during this storm event, as described previously. Finally, in all three cases, the time response of the modeled thermospheric temperature increase closely matches the measured density perturbation.

[33] There are also some striking differences in the three data sets. For example, the temporal evolution of the velocity and density fluctuations has significant features that differ between events, as seen by comparing the second and the third panels of Figures 1, 3, and 4. The measured neutral velocity perturbation in the satellite frame peaks very soon after storm onset in the August data, and is nearly coincident in time with the density increase. In September and October the velocity perturbation occurs later, well after the density perturbation. The maximum magnitudes of the velocity changes are comparable in the September and October data, but much larger in August. The time constant for recovery from the density perturbation is shorter for the September storm, but still closely mimics the modeled thermospheric density change. As a final qualitative observation, it is noteworthy that the density perturbation during the October storm displays a classical impulse response with an exponential-like recovery, while the other two cases have a plateau region in their density perturbation responses. However, we note that we have not attempted to model and remove the quiescent diurnal variation in our perturbation measurements. Doing so could introduce a change in the shape of the response, but would not affect the timing of the $\Delta N/N$ and ΔU responses, which are two of the primary variables of interest in this paper.

[34] An interesting feature of all three data sets is how quickly the equatorial thermosphere responds to the onset of the storm. The level of agreement between the modeled temperature changes and the measured density changes underscores this, since the drivers for the model are energy inputs in the high latitude region, and the independent *in situ* measurements are from the equatorial region. Since the energy is deposited at high latitudes, this quick response is indicative of a relatively fast coupling mechanism from high to low latitudes. It has been postulated by other authors [*Liu and Luhr*, 2005] that traveling atmospheric disturbances (TADs) are responsible for this transfer of heat. If this is the case, and if we assume that the high latitude heating occurs near 65° latitude, then the resultant propagation velocity is ~200 m/s. This is comparable to the thermal speed of neutral oxygen at these altitudes, and about twice as large as the perturbation velocities measured by the satellite near the

equator and shown in Figures 1, 3, and 4. Radiation is not an efficient heat transfer mechanism in this altitude domain. If advection were responsible, then $\Delta N/N$ and ΔU would increase simultaneously. This occurs for the August storm, but does not hold in September or October. The other possibility is conduction, which occurs at the thermal speed and is therefore in agreement with the time lags between the measured increases in $\Delta N/N$ and ΔU for the September and October storms.

[35] Although our data are single-point *in situ* measurements near the equator that cannot yield any definitive information on the manner in which heat is propagated through the thermosphere, it is possible to speculate along these lines. In our view, the most accurate physical picture of the heat transfer mechanism may not be a wave at all, but rather an expanding phase front that spreads equatorward from both auroral zones by conduction. The speed at which the heat transfer occurs would maximize at an altitude close to the height where the precipitation of energetic particles deposits most of the storm energy, and where the thermal conductivity of the gas is highest. In this picture, there is no classical oscillatory wave motion, but rather an envelope of expanding gas that progresses equatorward as the heat energy couples conductively. Detailed simulations of heat transfer in the thermosphere would be necessary to study this issue rigorously, but the fact that our observations show marked increases in the density at all longitudes (but over a limited range of local time) provides reasonably strong evidence that the equatorward propagation of heat is a global phenomenon. The idea that more localized TADs could produce synchronized heating at all longitudes seems unlikely in light of our observations.

[36] Regardless of how the energy spreads to equatorial latitudes, the measured equatorial density increases are likely associated with scale height changes induced by local thermospheric heating. We assume that the atmosphere is in hydrostatic equilibrium prior to the onset of the storm, which is likely true for the September and October storms, but is questionable for August when the perigees are near the sunset terminator. Starting from this equilibrium, the thermospheric heating caused by a storm increases the temperature and the scale height. As the higher temperature phase front moves equatorward from the auroral regions, the heated neutral atmosphere expands upward, resulting in increased pressures and particle densities at the altitude of the satellite observations. A simple calculation provides a consistency check that supports this idea. If N represents the neutral density, H is the scale height, T is the neutral temperature, and z represents the altitude above the reference level where the neutral density is N_0, then hydrostatic equilibrium requires

$$N(z) = N_0 \exp(-z/H). \quad (1)$$

[37] The variables of interest are the normalized perturbation quantities, since these are the parameters plotted in Figures 1, 3, and 4, and most reliably calculated from our data without invoking additional assumptions. If the subscript D is used to designate a disturbed quantity, and Q is used to designate the quiescent background level, then the dimensionless quantities of interest are $\delta N = (N_D - N_Q)/N_Q$ and $\delta T = (T_D - T_Q)/T_Q$. In terms of these variables, equation 1 leads to

$$\delta N = \exp(z\delta T/H_D) - 1. \quad (2)$$

[38] The δN and δT terms in equation 2 correspond to the quantities plotted in the second and fourth panels of Figures 1, 3, and 4. The average value of δN is near one for the three storms, while the average model value of the quiescent neutral temperatures is approximately 880 K, and δT is equal to 0.23. Assuming monatomic oxygen as the dominant neutral gas in the thermosphere gives $H_D \approx 64$ km. Plugging these observed and modeled values into equation 2 allows us to solve for z, the difference between the height of the *in situ* observations and the upper limit altitude at which the heat is efficiently transferred in the thermosphere. Carrying out this calculation yields $z = 200$ km, which implies that heat transfer in the thermosphere during these storms is most efficiently occurring at altitudes more than 200 km below the perigee of the satellite (~400 km), i.e., below 200 km altitude. This compares very favorably with both the modeling work of *Deng et al.* [2011] and the empirically guided calculations of *Thayer and Semeter* [2004]. Both of these studies show that thermospheric heating due to electromagnetic energy input is most efficient below 200 km altitude. Thus, in an average sense, the observations presented here are consistent with the hypothesis that energy propagates from high to low latitude regions at a velocity near the neutral thermal speed, enhancing the neutral gas temperature and modifying the scale height in the thermosphere, thereby causing the density increases observed by the satellite at perigee.

[39] The significance of the simple calculation above should not be overestimated, for several important reasons. First, it considers averages of all three storms despite the fact that the satellite samples different local times during each storm. It must also be recognized that composition changes are likely during storms, and changes in the O/N_2 ratio at the altitudes of the observations would have significant effects on the scale height. The instrumentation aboard the satellite does not measure neutral composition, so it is not possible to investigate this possibility for any of the storms. Finally, the comparison of ground-based and *in situ* measurements is not entirely appropriate, because the satellite samples all longitudes over each storm interval while the ground-based data measure local time variations at a fixed location. Nevertheless, the fact that the calculated and modeled data are consistent with energy transfer in the low-latitude thermosphere below 200 km provides a consistency check between disparate observations and helps to validate the measurements made by the CINDI neutral wind instrumentation.

7. Summary and Conclusions

[40] *In situ* perturbation densities and velocities in the thermosphere measured near 400 km during three fall storms in 2011 have similar signatures. The most significant findings from these observations include the following:

[41] 1. The storms show marked neutral density increases at satellite perigee altitudes ~5–7 h after the onset of the first

B_z oscillations, and significant equatorward surges in the neutral velocity coincident with or a few hours after the $\Delta N/N$ perturbations;

[42] 2. the perturbations in the neutral density near the equator range from about 50–100% relative to the pre-storm quiescent background;

[43] 3. the perturbation velocities are consistently equatorward and have peak responses near 100 m/s;

[44] 4. the time delays observed between the onset of the storm and the perturbations measured at low latitudes are consistent with propagation of energy from the auroral zone to the equatorial region at or very near the thermal speed for monatomic oxygen at 400 km altitude;

[45] 5. a two-step empirical model [*Weimer*, 2005b; *Bowman et al*., 2008] of low latitude thermospheric responses to storms yields temperature estimates that are consistent with the density perturbations observed at the 400 km perigee altitudes reached by the satellite;

[46] 6. the model temperature estimates are also in agreement with the Fabry-Perot observations made during the storms by the RENOIR and SOFDI systems on the South American continent; and

[47] 7. the velocity and density perturbations measured aboard the satellite occur almost simultaneously for two of the storms, but the velocity perturbation occurs somewhat later in the case where the satellite sampling was limited to local times in the early afternoon period.

[48] Previous satellite observations have documented the changes in thermospheric density and temperature as a function of latitude, but the measurements shown here are the first from a low inclination satellite, so the data presented herein emphasize changes occurring near the equator, but necessarily mix longitudinal and local time effects. However, the fact that these satellite observations cover all longitudes over a small range of local times for each storm indicates that the observed changes in temperature, density, and velocity are global in nature.

[49] It is likely that sophisticated numerical modeling tools will be needed to reconcile these and other satellite and ground-based observations with heat transfer mechanisms and global wind systems in order to obtain a deeper understanding of the global-scale changes wrought by magnetic storms.

[50] **Acknowledgments.** This work was supported by NASA grant NNX10AT02G. Robert Lysak thanks Gordon Shepherd and another reviewer for their assistance in evaluating this paper.

References

Balan, N., M. Yamamoto, J. Y. Liu, Y. Otsuka, H. Liu, and H. Luhr (2011), New aspects of thermospheric and ionospheric storms revealed by CHAMP, *J. Geophys. Res.*, *116*, A07305, doi:10.1029/2010JA016399.

Bowman, B. R., W. K. Tobiska, F. A. Marcos, C. Y. Huang, C. S. Lin, and W. J. Burke (2008), A new empirical thermospheric density model JB2008 using new solar and geomagnetic indices, Paper 2008, 6438, Am. Inst. of Aeronaut. and Astronaut., New York.

Deng, Y., T. J. Fuller-Rowell, R. A. Akmaev, and A. J. Ridley (2011), Impact of the altitudinal Joule heating distribution on the thermosphere, *J. Geophys. Res.*, *116*, A05313, doi:10.1029/2010JA016019.

Drob, D. P., et al. (2008), An empirical model of the Earth's horizontal wind fields: HWM07, *J. Geophys. Res.*, *113*, A12304, doi:10.1029/2008JA013668.

Earle, G. D., and M. C. Kelley (1987), Spectral studies of the sources of ionospheric electric fields, *J. Geophys. Res.*, *92*, 213.

Earle, G. D., et al. (2010), A comprehensive rocket and radar study of midlatitude spread F, *J. Geophys. Res.*, *115*, A12339, doi:10.1029/2010JA015503.

Fuller-Rowell, T. J., M. V. Codrescu, R. J. Moffet, and S. Quegan (1994), Response of the thermosphere and ionosphere to geomagnetic storms, *J. Geophys. Res.*, *99*, 2893.

Gerrard, A. J., and J. W. Meriwether (2011), Initial daytime and nighttime SOFDI observations of thermospheric winds from Fabry-Perot Doppler shift measurements of the 630-nm OI line-shape profile, *Ann. Geophys.*, *29*, 1529, doi:10.5194/angeo-29-1529-2011.

Gonzales, C. A., M. C. Kelley, B. G. Fejer, J. F. Vickrey, and R. F. Woodman (1979), Equatorial electric fields during magnetically disturbed conditions. 2. Implications of simultaneous auroral and equatorial measurements, *J. Geophys. Res.*, *84*, 5803.

Haaser, R. A., G. D. Earle, R. A. Heelis, W. R. Coley, and J. H. Klenzing (2010), Low-latitude measurements of neutral thermospheric helium dominance near 400 km during extreme solar minimum, *J. Geophys. Res.*, *115*, A11318, doi: 10.1029/2010JA015325.

Haines, G. V. (1985), Spherical cap harmonic analysis, *J. Geophys. Res.*, *90*, 2583.

Hanson, W. B., U. Ponzi, C. Arduini, and M. DeRuscio (1992), A satellite anemometer, *J. Astro. Sci.*, *40*, 429.

Hapgood, M. A. (1992), Space physics coordinate transformations: A user guide, *Planet. Space Sci.*, *40*(5), 711.

Hedin, A. E. (1991), Extension of the MSIS thermosphere model into the middle and lower atmosphere, *J. Geophys. Res.*, *96*(A2), 1159-1172.

Liu, H., and H. Luhr (2005), Strong disturbance of the thermospheric density due to storms: CHAMP observations, *J. Geophys. Res.*, *110*, A09529, doi:10.1029/2004JA010908.

Makela, J. J., M. C. Kelley, S. A. Gonzalez, N. Aponte, and R. P. McCoy (2001), Ionospheric topography maps using multiple wavelength all-sky images, *J. Geophys. Res.*, *106*, 29,161, doi:10.1029/2000JA000449.

Makela, J. J., J. W. Meriwether, J. P. Lima, E. S. Miller, and S. J. Armstrong (2009), The remote equatorial nighttime observatory of ionospheric regions project and the international heliophysical year, *Earth Moon Planet*, *104*, 211, doi:10.1007/s11038-008-9289-0.

Makela, J. J., J. W. Meriwether, Y. Huang, and P. J. Sherwood (2011), Simulation and analysis of a multi-order imaging Fabry-Perot interferometer for the study of thermospheric winds and temperatures, *Appl. Optics*, *50*(22), 4403.

Meriwether, J. W., J. J. Makela, Y. Huang, D. J. Fisher, R. A. Buriti, A. F. Medeiros, and H. Takahashi (2011), Climatology of the nighttime equatorial thermospheric winds and temperatures over Brazil near solar minimum, *J. Geophys. Res.*, *116*, A04322, doi: 10.1029/2011JA016477.

Rastogi, R. G. (1977), Geomagnetic storms and electric fields in the equatorial ionosphere, *Nature*, *268*, 422.

Richmond, A. D. (1995), Ionospheric electrodynamics using magnetic apex coordinates, *J. Geomag. Geoelectr.*, *47*, 191–212.

Solomon, S. C., and V. J. Abreu (1989), The 630 nm dayglow, *J. Geophys. Res.*, *94*, 6817–6824, doi:10.1029/JA094iA06p06817.

Thayer, J. P., and J. Semeter (2004), The convergence of magnetospheric energy flux in the polar atmosphere, *J. Atmos. Sol. Terr Phy.*, *66*(10), 805–822, doi:10.1016/j.jastp.2004.01.035.

Weimer, D. R. (2001), Maps of field-aligned currents as a function of the interplanetary magnetic field derived from Dynamics Explorer 2 data, *J. Geophys. Res.*, *106*, 12,889.

Weimer, D. R. (2005a), Improved ionospheric electrodynamic models and application to calculating Joule heating rates, *J. Geophys. Res.*, *110*, A05306, doi:10.1029/2004JA010884.

Weimer, D. R. (2005b), Predicting surface geomagnetic variations using ionospheric electrodynamic models, *J. Geophys. Res.*, *110*, A12307, doi:10.1029/2005JA011270.

Weimer, D. R., B. R. Bowman, E. K. Sutton, and W. K. Tobiska (2011), Predicting global average thermospheric temperature changes resulting from auroral heating, *J. Geophys. Res.*, *116*, A01312, doi:10.1029/2010JA015685.

Zhang, S. P., and G. G. Shepherd (2004), Solar influence on the O(1D) dayglow emission rate: Global-scale measurements by WINDII on UARS, *Geophys. Res. Lett.*, *31*, L07804, doi:10.1029/2004GL019447.